Monthly Notices
of the
ROYAL ASTRONOMICAL SOCIETY

MNRAS **492,** 39–44 (2020)
Advance Access publication 2019 December 12

doi:10.1093/mnras/stz3422

The origin of slow Alfvénic solar wind at solar minimum

D. Stansby [1★†], L. Matteini [1,2], T. S. Horbury [1], D. Perrone [1,3], R. D'Amicis [3] and L. Berčič [2,4]

[1] *Department of Physics, Imperial College London, London SW7 2AZ, UK*
[2] *LESIA, Observatoire de Paris, Université PSL, CNRS, Sorbonne Université, Univ. Paris Diderot, Sorbonne Paris Cité, 5 place Jules Janssen, F-92195 Meudon, France*
[3] *INAF - IAPS, Via Fosso del Cavaliere 100, 00133 Rome, Italy*
[4] *Physics and Astronomy Department, University of Florence, Via Giovanni Sansone 1, I-50019 Sesto Fiorentino, Italy*

Accepted 2019 December 3. Received 2019 December 2; in original form 2019 July 3

ABSTRACT

Although the origins of slow solar wind are unclear, there is increasing evidence that at least some of it is released in a steady state on overexpanded coronal hole magnetic field lines. This type of slow wind has similar properties to the fast solar wind, including strongly Alfvénic fluctuations. In this study, a combination of proton, alpha particle, and electron measurements are used to investigate the kinetic properties of a single interval of slow Alfvénic wind at 0.35 au. It is shown that this slow Alfvénic interval is characterized by high alpha particle abundances, pronounced alpha–proton differential streaming, strong proton beams, and large alpha-to-proton temperature ratios. These are all features observed consistently in the fast solar wind, adding evidence that at least some Alfvénic slow solar wind also originates in coronal holes. Observed differences between speed, mass flux, and electron temperature between slow Alfvénic and fast winds are explained by differing magnetic field geometry in the lower corona.

Key words: Sun: heliosphere – solar wind.

1 INTRODUCTION

The solar wind is an ionized plasma flowing at large speeds from the surface of the Sun to the edge of the Heliosphere. Although the density, speed, and temperature of the solar wind are all highly variable, it is possible to identify categories of solar wind with distinct properties. The most clearly defined category is that with the highest speeds, typically called the fast solar wind. Comparison between remote observations and *in situ* measurements shows that fast solar wind originates in large coronal holes spanning over 60° in angular width (Krieger, Timothy & Roelof 1973; Nolte et al. 1976; Cranmer 2009; Garton, Murray & Gallagher 2018).

In contrast, the solar sources of wind with slow and intermediate speeds are varied and still not entirely clear (e.g. see the review of Abbo et al. 2016). There are, however, multiple lines of evidence that a significant fraction of the slow solar wind also originates in coronal holes. One of the defining features of fast solar wind is a lack of variance in number density, velocity, and temperature, aside from pure Alfvénic fluctuations, which result in magnetic field and velocity variations that are either strongly correlated or anticorrelated (Belcher & Davis 1971; Bame et al. 1977). A steady background state with superimposed Alfvén waves is also observed *in situ* in a large amount of the slower solar wind at all stages of the solar cycle (Marsch et al. 1981; D'Amicis & Bruno 2015; Stansby, Horbury & Matteini 2019b), implying that close to the Sun it may also be heated and released into the heliosphere in a steady-state manner on open field lines.

One significant difference between the regions of coronal holes that are thought to produce slow and fast winds is the magnetic field geometry in the corona. The amount of magnetic field expansion alters the location of the critical point where the plasma becomes supersonic (Cranmer 2005), which in turn alters the effects of heating processes. If the majority of heating happens below the critical point, the speed is not significantly affected, whereas significant heating above the critical point is expected to increase the speed (Leer & Holzer 1980). Because rapidly diverging magnetic fields have a higher critical point, more energy is deposited before the wind becomes supersonic, thus resulting in slower wind speeds (Levine, Altschuler & Harvey 1977; Leer & Holzer 1980; Wang & Sheeley 1991).

These theoretical predictions agree well with an observed anti-correlation between solar wind speed at 1 au and the amount of superradial expansion the magnetic field undergoes close to the Sun (Wang & Sheeley 1990, 2006; Suzuki 2006; Fujiki et al. 2015).

★ E-mail: d.stansby@ucl.ac.uk
† Present address: Mullard Space Science Laboratory, University College London, Holmbury St. Mary, Surrey RH5 6NT, UK.

Table 1. Start and end times for selected intervals. All data are taken from *Helios 1*.

Category	Start time (UT)	End time (UT)
Fast	1975/03/13 12:00	1975/03/16 12:00
Slow Alfvénic	1975/03/23 00:00	1975/03/24 16:00
Slow non-Alfvénic	1975/03/25 14:00	1975/03/26 00:00

Statistically the smallest coronal holes, with the highest magnetic field expansions, produce wind with the slowest speeds (Nolte et al. 1976; Garton et al. 2018; Hofmeister et al. 2018), which has been verified on a case-by-case basis using magnetic field mappings from spacecraft to the solar surface (Wang, Ko & Grappin 2009; Wang 2017; Wang & Ko 2019). In addition, case studies at 1 au show that the slow Alfvénic wind contains similar heavy ion composition (D'Amicis, Matteini & Bruno 2018), and similar alpha-to-proton abundance ratios (Ohmi et al. 2004) as fast solar wind, reinforcing a probable similar solar origin. These previous studies have shown that the bulk properties of the slow Alfvénic wind are consistent with the theory that it originates in open field lines rooted in coronal holes.

If this theory is true, one would expect the processes occurring as the solar wind is heated and accelerated to be similar in both the fast and slow Alfvénic wind, and thus expect similar features to be found in the velocity distribution functions in both types of wind. The kinetic features of fast solar wind have been extensively characterized: it contains a proton beam population (Feldman et al. 1973, 1993), large alpha particle to proton temperature ratios (Marsch et al. 1982a; Stansby et al. 2019c), magnetic-field-aligned proton–alpha particle streaming (Marsch et al. 1982a; Neugebauer et al. 1996), and large alpha-to-proton abundance ratios (Aellig, Lazarus & Steinberg 2001; Kasper et al. 2007). Marsch et al. (1982b) and D'Amicis et al. (2018) have shown that at 1 au both fast and slow Alfvénic winds tend to have isotropic proton distributions, but the other features have yet to be measured in slow Alfvénic wind.

In this paper, we provide the first observations of these kinetic features in both slow and fast Alfvénic winds. Some of these features are destroyed by the time the solar wind has propagated to 1 au, necessitating the use of data from the *Helios* mission, which measured the solar wind from 0.3–1 au. Three intervals are studied, initially identified by Stansby et al. (2019b) as (a) typical fast solar wind, (b) Alfvénic slow solar wind, and (c) non-Alfvénic slow solar wind. Our comparison of both the bulk and kinetic features of fast and slow Alfvénic intervals shows that the slow Alfvénic period most likely originated from a small, overexpanded coronal hole.

2 DATA

The data used here were measured by the *Helios* mission, which consisted of two spacecraft in heliocentric orbits between 0.3 and 1 au (Porsche 1977). The first perihelion pass of *Helios 1* during solar minimum was used, from which three periods were chosen as representative examples of fast, slow Alfvénic, and slow non-Alfvénic wind. The intervals are listed in Table 1 and shown later in Fig. 2, and were chosen to contain continuous alpha particle measurements and to be long enough to build up a statistical characterization of each interval.

Particle data were measured by the E1 set of instruments, consisting of electrostatic analysers for both ions and electrons (Schwenn, Rosenbauer & Miggenrieder 1975). Magnetic field data were measured by both the E2 and E3 fluxgate magnetometers (Musmann et al. 1975; Scearce et al. 1975). Where possible, magnetic field data from E2 were used, with E3 data as a fallback. Although data gaps are frequent, the particle data are available at a maximum cadence of 40.5 s, and magnetic field measurements used here were averaged over the time taken to build up each individual particle distribution function.

Alpha particle parameters were calculated using the bi-Maxwellian fitting routine described in appendix A of Stansby et al. (2019c), with minor modifications to adapt the fitting to work well in both slow and fast solar winds[1]. Proton temperatures and velocities are bi-Maxwellian fits to the proton core from the data set of Stansby et al. (2018)[2]. Electron core parameters were obtained using the method presented in Berčič et al. (2019), also calculated with a bi-Maxwellian fitting routine. For each species, the fitted parameters are number density (n_i), velocity ($\mathbf{v}_i$), and temperatures perpendicular and parallel to the local magnetic field ($T_{i\perp}$, $T_{i\parallel}$). The subscript i is substituted as p for protons, α for alpha particles, or e for electrons.

Example ion energy spectra for each interval, along with their corresponding proton and alpha particle fits, are shown in Fig. 1, demonstrating that the fitting works well in all types of wind. In both the proton and alpha parts of the distribution function a high-energy tail or 'beam' is present (e.g. Feldman et al. 1973; Marsch et al. 1982a,b) that by design is not captured by these fits to the core parts of the distribution function.

Energy per charge units (measured directly by the instrument) can be converted to velocity for a given particle species by

$$\sqrt{\frac{E}{q}} = v\sqrt{\frac{m}{2q}}, \tag{1}$$

where m and q are the particle mass and electromagnetic charge, respectively. Because of their increased charge-to-mass ratio, in these plots alpha particles appear at $\sqrt{E/q}$ values a factor of $\sqrt{2}$ higher than protons travelling at the same speed.

In Fig. 1, some differences are already apparent between the three types of wind. The fast (top panel) and the slow Alfvénic (bottom left panel) wind show a similar structure, with a proton core population, an additional proton beam population (not captured by the fits, but characterized later), and an alpha particle distribution which is wider and therefore significantly hotter than the proton distribution. In contrast, the slow non-Alfvénic wind (bottom right panel) has no obvious proton beam, and a much thinner alpha particle distribution than the other types of wind.

In order to characterize the extra beam population of protons, the beam number density was calculated as the numerical integral

$$n_\mathrm{b} = \iiint \left[f_\mathrm{obs}\left(\boldsymbol{v}\right) - f_\mathrm{bimax}\left(\boldsymbol{v}\right)\right] \mathrm{d}\boldsymbol{v}, \tag{2}$$

where f_obs is the observed velocity distribution function, f_bimax is the fitted bi-Maxwellian core distribution function, and the integral is taken over the 3D velocity space with upper integration limit in $|\mathbf{v}|$ set to exclude the areas of f_obs dominated by alpha particles. Unless otherwise stated, the total proton number density (n_p) is the sum of the proton core and beam number densities.

Aside from the aforementioned basic plasma parameters, some derived parameters are used later, which are defined as follows:

[1]The updated fitting routine can be found at https://github.com/dstansby/alphafit, and the newly calculated parameters at https://doi.org/10.5281/zenodo.3560879.

[2]Available at https://doi.org/10.5281/zenodo.1009506.

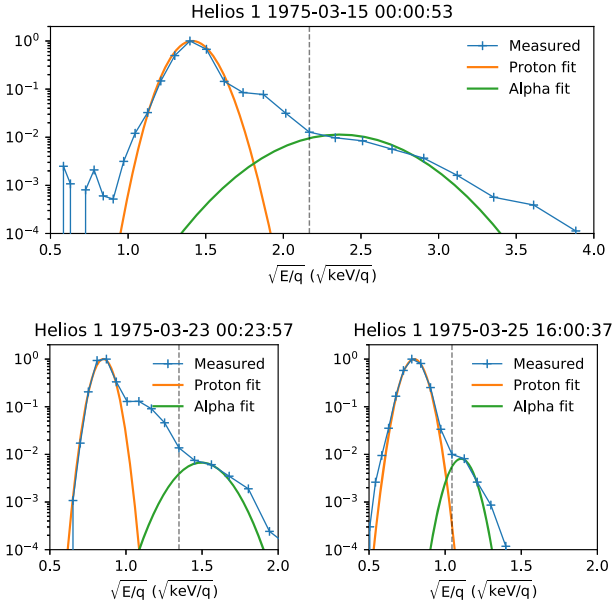

Figure 1. Example energy spectra (blue crosses) measured in each type of solar wind. The top panel shows fast wind, bottom left slow Alfvénic wind, and the bottom right shows slow non-Alfvénic wind. The solid-angle-integrated bi-Maxwellian fits are shown for protons (orange line) and alpha particles (green line). The vertical grey line shows the dividing line between measurements dominated by protons (to the left) and those dominated by alpha particles (to the right). Note that the fits are performed in the full 3D velocity space, and shown here are 1D reductions of the distribution functions and fits.

(i) The Alfvénic speed is

$$v_{\rm A} = \frac{|\boldsymbol{B}|}{\sqrt{\mu_0 \rho}}, \tag{3}$$

where $\rho = \sum_i n_i m_i$ is the total mass density of the plasma (including the proton beam).

(ii) The proton beam fraction is

$$\frac{n_{\rm b}}{n_{\rm p}} = \frac{n_{\rm b}}{n_{\rm pc} + n_{\rm b}}, \tag{4}$$

where $n_{\rm pc}$ is the proton core number density calculated from bi-Maxwellian fits.

Finally, as a proxy for the Alfvénicity of the plasma, the cross-helicity ($\sigma_{\rm c}$) calculated from multiple measurements is used. This is defined as (Bruno & Carbone 2013)

$$\sigma_{\rm c} = 2\frac{\langle \boldsymbol{v} \cdot \boldsymbol{b} \rangle}{\langle |\boldsymbol{v}|^2 + |\boldsymbol{b}|^2 \rangle} \tag{5}$$

and is calculated in the same manner as Stansby et al. (2019b). $\boldsymbol{v} = \boldsymbol{v}_p - \boldsymbol{v}_{p0}$ are the proton velocity fluctuations in the Alfvén wave frame, $\boldsymbol{v}_{p0}$ is chosen to maximize the value of $|\sigma_{\rm c}|$, and $\boldsymbol{b} = v_{\rm A}(\boldsymbol{B}/|\boldsymbol{B}|)$ is the magnetic field in velocity units. The time averages denoted by $\langle\rangle$ are taken over all points in non-overlapping 20 min windows. Uncertainties in $\sigma_{\rm c}$ calculated with a bootstrap method are always less than ± 0.1 and almost always less than ± 0.05.

3 RESULTS

Fig. 2 presents an overview of the first perihelion pass of *Helios 1* in early 1975. This shows a typical solar minimum structure in the ecliptic plane, with several fast coronal hole streams interspersed with slower wind speed periods.

The intervals listed in Table 1 are shown with coloured vertical bands in Fig. 2, and are examples of fast (grey), slow Alfvénic (blue), and slow non-Alfvénic (red) wind. The choice of intervals was primarily motivated by the need to have enough alpha particle measurements to carry out the later statistical analysis. Note that the slow Alfvénic stream begins after clear discontinuities in proton number density and temperature, and is clearly distinct from the trailing edge of the preceding high-speed stream. Both the fast and slow Alfvénic periods have very high Alfvénicities, with $|\sigma_{\rm c}| > 0.9$, whereas the non-Alfvénic wind is characterized by a large scatter of $|\sigma_{\rm c}|$ values between 0 and 1.

Fig. 3 shows histograms of various parameters in each type of wind, using the same interval colour coding as Fig. 2. Panel (a) shows the proton radial velocity, making clear that the slow Alfvénic wind has significantly slower speeds (~400 km s^{-1}) than the fast wind (~600 km s^{-1}). Panel (b) shows the alpha particle flux, normalized to the proton flux ($v_{\alpha r} n_\alpha / v_{\rm pr} n_{\rm p}$). Note that the relative flux is plotted instead of the relative abundance, since the abundance is not conserved if the alpha particle and proton velocities change, whereas the flux is conserved (Hollweg 1974; Wang 2008). At these distances the relative fluxes and abundances are similar, however, due to relatively similar proton and alpha particle radial speeds. The slow Alfvénic wind has similar relative alpha particle fluxes to the fast solar wind (~0.05), whereas the non-Alfvénic wind has significantly smaller fluxes, as shown previously (for another interval) by Ohmi et al. (2004). Panel (c) shows the proton number density flux, normalized to radial distance (i.e. particles per second per solid angle). The slow Alfvénic wind has a flux around twice that of the fast wind, and the non-Alfvénic wind has large fluxes around four times the fast wind flux. Panel (d) shows the electron perpendicular temperature, which in the slow Alfvénic wind (0.2 MK) is twice that of the fast wind (0.1 MK), but slightly cooler than the non-Alfvénic wind (0.25 MK). Panel (e) shows the proton beam fraction. The non-Alfvénic wind has a low proton beam fraction (<5 per cent), in contrast to the fast wind (~7 per cent), whereas the slow Alfvénic wind has a significantly higher beam fraction at ~18 per cent. This agrees well with previous estimates of the beam fraction from *Helios*, showing that when a proton beam is present, it has a higher relative density in slower wind (Marsch et al. 1982b). Panel (f) shows the alpha particle streaming speed. In agreement with previous studies (e.g. Marsch et al. 1982a; Neugebauer et al. 1996), alphas stream at a significant fraction of the Alfvén speed in the fast solar wind, and the alpha particles also stream at a slightly smaller but still significant fraction in the slow Alfvénic wind (as also shown for another interval by Marsch et al. 1981). The non-Alfvénic wind has an average proton–alpha drift speed close to zero, which may be due to its relatively high collisionality (due to a high density and low temperature). Finally, panels (g) and (h), respectively, show the proton and alpha particle temperature anisotropy. The non-Alfvénic wind is isotropic for both particle populations, again most likely due to a high collisionality. The sense of temperature anisotropy is the same in the fast and slow Alfvénic winds, with $T_\perp > T_\parallel$ for protons but $T_\perp < T_\parallel$ for alpha particles, however the proton temperature anisotropy is weaker in the slow Alfvénic wind compared to the fast wind (see also Stansby et al. 2019b). Note that at least in the fast wind, these features in alpha particle temperatures are not observable at 1 au, due to the effect of plasma micro-instabilities on the evolution of alpha particle temperatures (Stansby et al. 2019c).

Fig. 4 shows the joint distributions of proton and alpha particle temperatures in each of the three types of wind, with the same colour coding as Fig. 3. The non-Alfvénic wind has $T_{\alpha\perp} \approx T_{\alpha\parallel}$

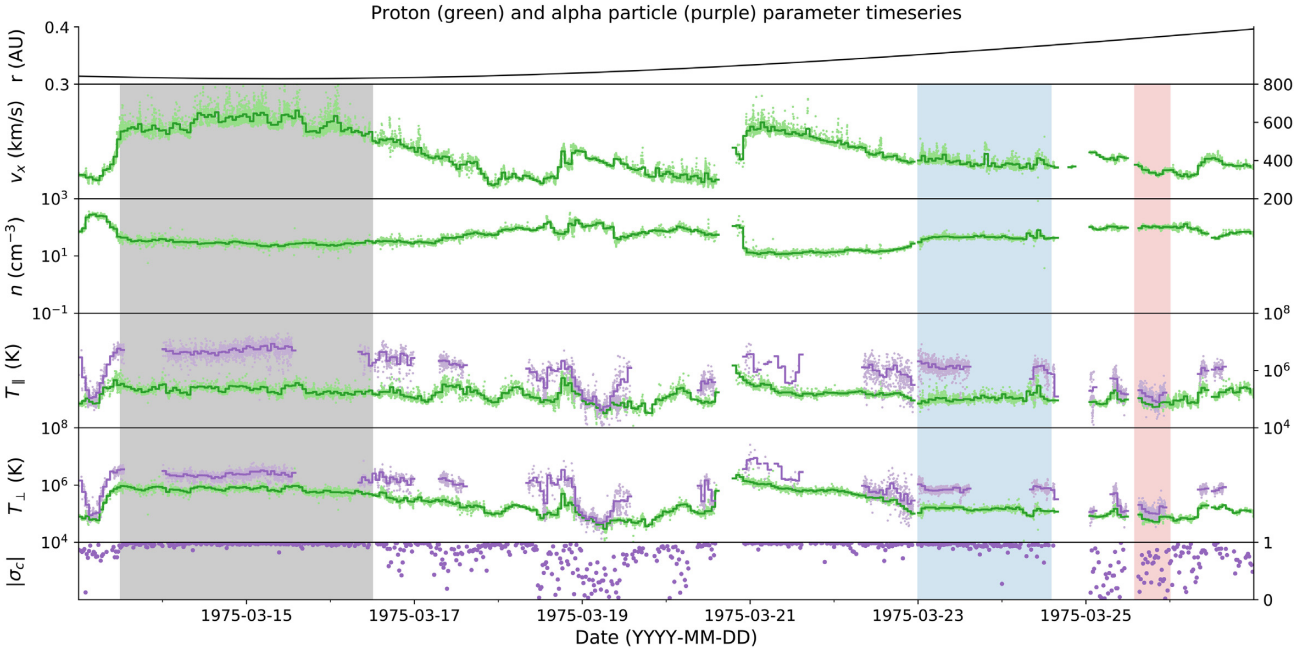

Figure 2. Proton (green) and alpha particle (purple) parameter time series from the first perihelion pass of *Helios 1*. From top to bottom: heliocentric distance, radial velocity, number density, parallel temperature, perpendicular temperature, and absolute cross-helicity. In the middle four panels, 40.5 s cadence measurements are shown with light dots, and hourly averaged parameters with dark lines.

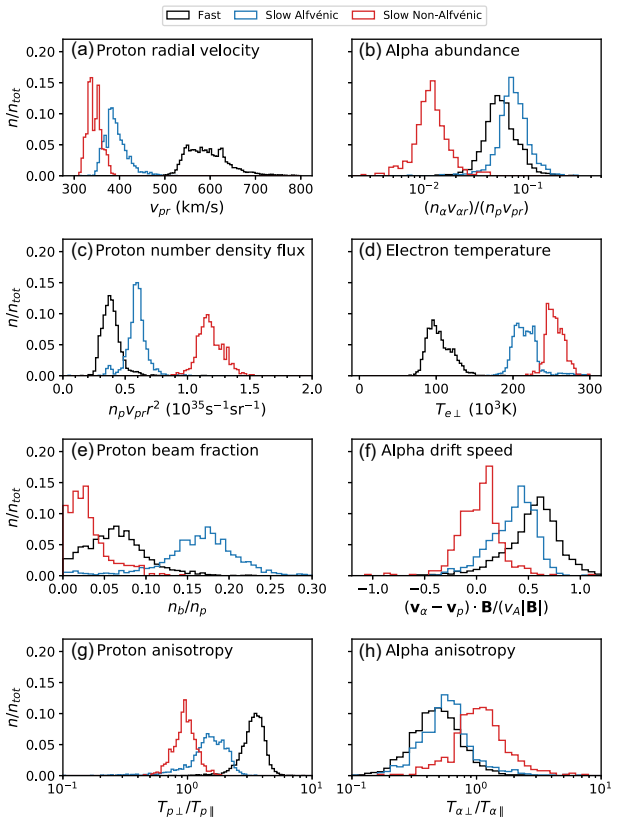

Figure 3. Histograms of various parameters in the three different intervals, normalized to the total number of data points in each interval.

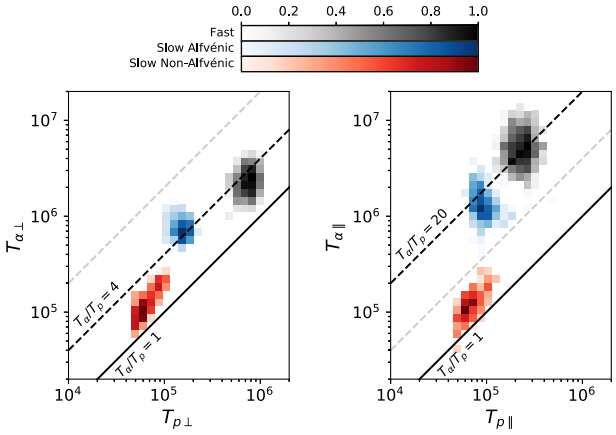

Figure 4. Joint distribution of magnetic field perpendicular (left-hand panel) and parallel (right-hand panel) proton and alpha particle temperatures in three types of solar wind. Distributions are normalized to the maximum bin value.

$\approx 10^5$ K. The similarity in proton and alpha particle temperatures here may again be due to the non-Alfvénic wind's relatively high collisionality. On the other hand, the slow Alfvénic wind has an order-of-magnitude larger alpha particle temperatures of $\sim 10^6$ K. The alpha-to-proton temperature ratios are similar in the fast and slow Alfvénic wind, in both the perpendicular ($T_{\alpha\perp} \approx 4T_{p\perp}$) and parallel ($T_{\alpha_{\parallel}} \approx 20T_{p_{\parallel}}$) directions.

4 DISCUSSION

The slow Alfvénic solar wind has similar alpha-to-proton number density fluxes as the fast solar wind (Fig. 3, panel b). Because alpha particles are heavier than protons, they require extra forces above

those that accelerate the protons acting on them in order to avoid gravitational settling reducing their abundance to significantly less than the photospheric abundance (Hansteen, Leer & Holzer 1994; Basu & Antia 1995; Asplund et al. 2009). Our results suggest that similar mechanisms driving these enhanced Helium fluxes are active in both the fast and slow Alfvénic solar winds, but not in the non-Alfvénic slow wind. More specifically, there must be mechanisms other than Coulomb friction, which alone would make the alpha abundance very sensitive to the proton number density flux (Geiss, Hirt & Leutwyler 1970), in contrast to these observations.

In addition, the slow Alfvénic and fast winds both have similar proton–alpha drift speeds (Fig. 3, panel f) and alpha-to-proton temperature ratios (Fig. 4). The proposed mechanisms to impart these properties include second-order effects of Alfvén waves (Hollweg 1974; Chang & Hollweg 1976), ion cyclotron wave acceleration (Hollweg & Isenberg 2002), or reconnection jets (Feldman et al. 1993, 1996). Although the observations presented here cannot distinguish between these different proposals, they suggest that similar mechanisms are active in both the fast and the slow Alfvénic wind.

The slow Alfvénic wind shows some differences to the fast wind however; it has slower speeds (Fig. 3, panel a), higher mass fluxes (Fig. 3, panel c), higher electron temperatures (Fig. 3, panel d), and lower overall proton and alpha temperatures (Fig. 4). These observations agree with the idea that both the fast and the slow Alfvénic solar wind were produced on open field lines rooted in coronal holes, but with varying magnetic field geometries in the lower corona. In particular, the amount the magnetic field expands in the low corona (up to $2.5r_{\odot}$), the footpoint magnetic field strength, and the magnetic field inclination at the solar surface are all thought to be important in shaping the properties of coronal hole wind (Suess et al. 1984; Wang & Sheeley 1990; Bravo & Stewart 1997; Suzuki 2006; Pinto, Brun & Rouillard 2016; Réville & Brun 2017).

The amount of magnetic field expansion sets the location of the critical point where the plasma becomes supersonic, with higher expansion factors resulting in higher Alfvénic points (Cranmer 2005; Cranmer, van Ballegooijen & Edgar 2007). This in turn alters the effects of heating processes. If heating happens while the wind is sub-Alfvénic, the mass flux is increased but the speed is not expected to be significantly affected; on the other hand, heating the wind while it is supersonic is expected to leave the mass flux unchanged but to increase the flow speed (Leer & Holzer 1980; Wang et al. 2009). This leads to more energy being deposited below the critical point for rapidly diverging magnetic fields, thus resulting in slower speeds but increased mass fluxes (Levine et al. 1977; Leer & Holzer 1980; Wang & Sheeley 1991), precisely as observed.

The lower ion temperatures in the slow Alfvénic wind agree with previous statistical observations of a positive correlation between proton bulk speed and both proton (Elliott et al. 2012) and alpha particle (Thieme, Marsch & Rosenbauer 1989) temperatures, and also agree with observations at 1 au of the slow Alfvénic wind at solar maximum (D'Amicis et al. 2018). Although the mechanisms behind this relation are still not clear, it is reproducible in steady-state models of the solar wind (Cranmer et al. 2007; Pinto & Rouillard 2017; Usmanov et al. 2018).

A striking feature of the slow Alfvénic wind is its large proton beam fraction (∼18 per cent) compared to the fast wind (∼7 per cent). Although the proton beam has been previously observed in case studies (e.g. Feldman et al. 1973, 1993), and its drift has been statistically characterized for *Helios* (Marsch et al. 1982b; Ďurovcová, Šafránková & Němeček 2019), at 1 au (Alterman et al. 2018), and beyond with *Ulysses* (Matteini et al. 2013), to our knowledge a large statistical study of proton beam fraction has yet to be carried out[3]. Such a study would be helpful in the future to determine what causes the observed large variations in proton beam fraction between different streams.

The higher electron temperatures in the slow Alfvénic wind with respect to the fast wind are also in agreement with previous observational *in situ* results at solar minimum, showing an anticorrelation between proton bulk speed and electron temperature inside 0.3 au (Marsch et al. 1989; Pilipp et al. 1990). A similar anticorrelation has been measured closer to the Sun, with remote sensing measurements showing relatively low electron temperatures above coronal holes where fast solar wind originates, compared to quiet Sun areas where some slow solar wind may originate (see section 12 of Del Zanna & Mason 2018, and references therein). In order to compare our *in situ* results to remote sensing measurements however, a study of coronal electron temperature differences between coronal holes of varying sizes would be needed, which to our knowledge does not yet exist.

Taken overall, our results provide new lines of evidence that a component of the slow solar wind originates in coronal holes, complementing other recent work that has come to a similar conclusion using different methods. Case studies of heavy ion charge state data measured at 1 au in the ecliptic plane show that slow Alfvénic wind has a similar composition to fast wind, implying a similar solar origin in coronal holes (D'Amicis et al. 2018). In addition, statistical studies of heavy ion fractionation measured at and beyond 1 au at a large range of solar latitudes show a significant fraction of slow solar wind with similarly low Fe/O ratios as fast wind, again implying that a significant fraction of the slow solar wind comes from overexpanded coronal holes (Stakhiv et al. 2015, 2016).

5 CONCLUSIONS

We have presented a detailed case study comparison between the kinetic properties of protons and alpha particles in the fast, slow Alfvénic, and slow non-Alfvénic solar winds using data taken by *Helios 1* during its first perihelion passage. The similarity in alpha particle abundance, alpha-to-proton temperature ratio, and alpha particle drift speed in the slow Alfvénic and fast winds adds additional evidence that some slow Alfvénic wind originates in coronal holes, similar to the fast solar wind. The differences in speed, mass flux, and electron temperatures between the slow Alfvénic and fast solar wind are explained by different magnetic field geometries in the low corona: the slower wind is released on magnetic field lines that undergo overexpansion that modifies the effects of coronal heating and acceleration processes.

An obvious next step would be performing a magnetic field connectivity analysis (e.g. Neugebauer et al. 1998) to determine if the observing spacecraft was really connected to a small coronal hole at the time of measurement. Unfortunately, to our knowledge, there are no magnetic field or extreme ultraviolet images of the Sun available for the interval studied in 1975. However, *Parker Solar Probe* (PSP; Fox et al. 2016) is predicted to have been connected to a small coronal hole during its first closest approach to the Sun (Riley et al. 2019). Having taken *in situ* measurements of the solar

[3]Marsch et al. (1982b) provide a statistical study of the radial variation of n_b/n_p, but only in cases where the proton beam appears as a distinct peak, therefore not including cases with a weak or non-existent beam.

wind down to 0.15 au, PSP will hopefully allow measurement of the kinetic features of solar wind unambiguously emitted from a small coronal hole during solar minimum.

ACKNOWLEDGEMENTS

The authors thank Roberto Bruno for helpful discussions, Marcia Neugebauer for comments and suggestions that significantly contributed to the results and discussion, and the referee for comments that improved discussion of our results. DS, TSH, and DP were supported by STFC grant ST/N000692/1. This work was supported by the Programme National PNST of CNRS/INSU co-funded by CNES.

The authors are grateful to the *Helios* and ACE instrument teams for making the data used in this study publicly available. Data were retrieved using HELIOPY v0.8.0 (Stansby et al. 2019a) and processed using ASTROPY v3.2.1 (Astropy Collaboration 2018). Figures were produced using MATPLOTLIB v3.1.1 (Hunter 2007).

Code to reproduce the figures presented in this paper is available at https://github.com/dstansby/publication-code.

REFERENCES

Abbo L. et al., 2016, Space Sci. Rev., 201, 55
Aellig M. R., Lazarus A. J., Steinberg J. T., 2001, Geophys. Res. Lett., 28, 2767
Alterman B. L., Kasper J. C., Stevens M. L., Koval A., 2018, ApJ, 864, 112
Asplund M., Grevesse N., Sauval A. J., Scott P., 2009, ARA&A, 47, 481
Astropy Collaboration, 2018, AJ, 156, 123
Bame S. J., Asbridge J. R., Feldman W. C., Gosling J. T., 1977, J. Geophys. Res., 82, 1487
Basu S., Antia H. M., 1995, MNRAS, 276, 1402
Belcher J. W., Davis L., 1971, J. Geophys. Res., 76, 3534
Bruno R., Carbone V., 2013, Living Rev. Sol. Phys., 10, 1
Berčič L., Maksimović M., Landi S., Matteini L., 2019, MNRAS, 486, 3404
Bravo S., Stewart G. A., 1997, ApJ, 489, 992
Chang S. C., Hollweg J. V., 1976, J. Geophys. Res., 81, 1659
Cranmer S. R., 2005, preprint (arXiv:astro-ph/0506508)
Cranmer S. R., 2009, Living Rev. Sol. Phys., 6, 3
Cranmer S. R., van Ballegooijen A. A., Edgar R. J., 2007, ApJS, 171, 520
D'Amicis R., Bruno R., 2015, ApJ, 805, 84
D'Amicis R., Matteini L., Bruno R., 2018, MNRAS, 483, 4665
Del Zanna G., Mason H. E., 2018, Living Rev. Sol. Phys., 15, 5
Ďurovcová T., Šafránková J., Němeček Z., 2019, Sol. Phys., 294, 97
Elliott H. A., Henney C. J., McComas D. J., Smith C. W., Vasquez B. J., 2012, J. Geophys. Res. Space Phys., 117, A09102
Feldman W. C., Asbridge J. R., Bame S. J., Montgomery M. D., 1973, J. Geophys. Res., 78, 2017
Feldman W. C., Gosling J. T., McComas D. J., Phillips J. L., 1993, J. Geophys. Res. Space Phys., 98, 5593
Feldman W. C., Barraclough B. L., Phillips J. L., Wang Y.-M., 1996, A&A, 316, 355
Fox N. J. et al., 2016, Space Sci. Rev., 204, 7
Fujiki K., Tokumaru M., Iju T., Hakamada K., Kojima M., 2015, Sol. Phys., 290, 2491
Garton T. M., Murray S. A., Gallagher P. T., 2018, ApJ, 869, L12
Geiss J., Hirt P., Leutwyler H., 1970, Sol. Phys., 12, 458
Hansteen V. H., Leer E., Holzer T. E., 1994, ApJ, 428, 843
Hofmeister S. J., Veronig A., Temmer M., Vennerstrom S., Heber B., Vršnak B., 2018, J. Geophys. Res. Space Phys., 123, 1738
Hollweg J. V., 1974, J. Geophys. Res., 79, 1357
Hollweg J. V., Isenberg P. A., 2002, J. Geophys. Res. Space Phys., 107, SSH12
Hunter J. D., 2007, Comput. Sci. Eng., 9, 90
Kasper J. C., Stevens M. L., Lazarus A. J., Steinberg J. T., Ogilvie K. W., 2007, ApJ, 660, 901
Krieger A. S., Timothy A. F., Roelof E. C., 1973, Sol. Phys., 29, 505
Leer E., Holzer T. E., 1980, J. Geophys. Res. Space Phys., 85, 4681
Levine R. H., Altschuler M. D., Harvey J. W., 1977, J. Geophys. Res., 82, 1061
Marsch E., Mühlhäuser K.-H., Rosenbauer H., Schwenn R., Denskat K. U., 1981, J. Geophys. Res., 86, 9199
Marsch E., Mühlhäuser K.-H., Rosenbauer H., Schwenn R., Neubauer F. M., 1982a, J. Geophys. Res., 87, 35
Marsch E., Mühlhäuser K.-H., Schwenn R., Rosenbauer H., Pilipp W., Neubauer F. M., 1982b, J. Geophys. Res., 87, 52
Marsch E., Pilipp W. G., Thieme K. M., Rosenbauer H., 1989, J. Geophys. Res. Space Phys., 94, 6893
Matteini L., Hellinger P., Goldstein B. E., Landi S., Velli M., Neugebauer M., 2013, J. Geophys. Res. Space Phys., 118, 2771
Musmann G., Neubauer F. M., Maier A., Lammers E., 1975, Raumfahrtforschung, 19, 232
Neugebauer M., Goldstein B. E., Smith E. J., Feldman W. C., 1996, J. Geophys. Res. Space Phys., 101, 17047
Neugebauer M. et al., 1998, J. Geophys. Res. Space Phys., 103, 14587
Nolte J. T. et al., 1976, Sol. Phys., 46, 303
Ohmi T., Kojima M., Tokumaru M., Fujiki K., Hakamada K., 2004, Adv. Space Res., 33, 689
Pilipp W. G., Miggenrieder H., Mühläuser K.-H., Rosenbauer H., Schwenn R., 1990, J. Geophys. Res., 95, 6305
Pinto R. F., Rouillard A. P., 2017, ApJ, 838, 89
Pinto R. F., Brun A. S., Rouillard A. P., 2016, A&A, 592, A65
Porsche H., 1977, J. Geophys., 42, 551
Réville V., Brun A. S., 2017, ApJ, 850, 45
Riley P., Downs C., Linker J. A., Mikic Z., Lionello R., Caplan R. M., 2019, ApJ, 874, L15
Scearce C., Cantarano S., Ness N., Mariani F., Terenzi R., Burlaga L., 1975, Raumfahrtforschung, 19, 237
Schwenn R., Rosenbauer H., Miggenrieder H., 1975, Raumfahrtforschung, 19, 226
Stakhiv M., Landi E., Lepri S. T., Oran R., Zurbuchen T. H., 2015, ApJ, 801, 100
Stakhiv M., Lepri S. T., Landi E., Tracy P., Zurbuchen T. H., 2016, ApJ, 829, 117
Stansby D., Salem C., Matteini L., Horbury T., 2018, Sol. Phys., 293, 155
Stansby D. et al., 2019a, Heliopython/Heliopy: HelioPy 0.8.0, Zenodo
Stansby D., Horbury T. S., Matteini L., 2019b, MNRAS, 482, 1706
Stansby D., Perrone D., Matteini L., Horbury T. S., Salem C. S., 2019c, A&A, 623, L2
Suess S. T., Wilcox J. M., Hoeksema J. T., Henning H., Dryer M., 1984, J. Geophys. Res. Space Phys., 89, 3957
Suzuki T. K., 2006, ApJ, 640, L75
Thieme K. M., Marsch E., Rosenbauer H., 1989, J. Geophys. Res., 94, 2673
Usmanov A. V., Matthaeus W. H., Goldstein M. L., Chhiber R., 2018, ApJ, 865, 25
Wang Y.-M., 2008, ApJ, 683, 499
Wang Y.-M., 2017, ApJ, 841, 94
Wang Y.-M., Ko Y.-K., 2019, ApJ, 880, 146
Wang Y.-M., Sheeley N. R. Jr, 1990, ApJ, 355, 726
Wang Y.-M., Sheeley N. R., 1991, ApJ, 372, L45
Wang Y.-M., Sheeley N. R., 2006, ApJ, 653, 708
Wang Y.-M., Ko Y.-K., Grappin R., 2009, ApJ, 691, 760

This paper has been typeset from a TEX/LATEX file prepared by the author.